POLITECNICO
MILANO 1863

SCUOLA DI INGEGNERIA INDUSTRIALE
E DELL'INFORMAZIONE

Executive Summary of the Thesis

The role of temperature and heavy ions irradiation in the microstructural evolution of amorphous alumina coating for LFR applications

Laurea Magistrale in Nuclear Engineering - Ingegneria Nucleare

Author: Giulio Fierli

Advisor: Prof. Marco Beghi

Co-advisor: Fabio Di Fonzo

Academic year: 2022-2023

1. Introduction

Lead-cooled fast reactors represent one of the most prominent technology of Generation IV nuclear reactors.These reactors offer numerous advantages, primarily attributed to their utilization of liquid lead as a coolant. However, the utilization of liquid lead or in some cases, lead-bismuth eutectic (LBE), implicates compatibility issues with structural materials, primarily steels. These challenges manifest in various forms such as liquid metal corrosion, liquid metal embrittlement and erosion, which must be addressed to ensure the reliable and safe operation of these reactors. One potential strategy to overcome these criticalities involves the application of coatings to physical separate reactor components from the coolant. Researchers from the CNST@Polimi at IIT have developed an innovative solution in the form of an amorphous alumina nanoceramic coating deposited using Pulsed Laser Deposition technology [2]. The coating, which demonstrates its optimal protective capabilities as long as the alumina remains in the amorphous phase, is exposed to both thermal and irradiation processes. The objective of this study is to explore two key aspects: first, how the microstructure of alumina evolves, and second, how the stability of the amorphous phase is influenced by modifying specific deposition parameters.

2. Experimental

2.1. Thermal Behavior

Alumina coating is deposited on an AISI 316L substrate, steel selected for its prominent role as structural components material in LFR. The samples produced differ for some deposition parameters, explicated in table 1.

Al20	Al_2O_3 deposited at 20 Hz without mask
Al50	Al_2O_3 deposited at 50 Hz with mask

Table 1: Set of samples undergone the thermal annealing.

Both types of sample underwent a thermal annealing in vacuum at temperatures of 600°C and 650°C with a dwelling time of 12 hours, values of temperatures selected for their vicinity to the crystallization temperature of alumina and with a margin to the operational conditions of an LFR. After the thermal treatment an XRD analysis is performed in order to gain a first insight

of the crystallization level of the coatings. Since the low thickness of the film and the grazing angle configuration, the peaks relative intensity results not reliable for a more quantitative evaluation of the amorphous fraction. Furthermore, to check the integrity of the films, an observation of the coating surface is carried out through SEM images. From the XRD pattern can be observed

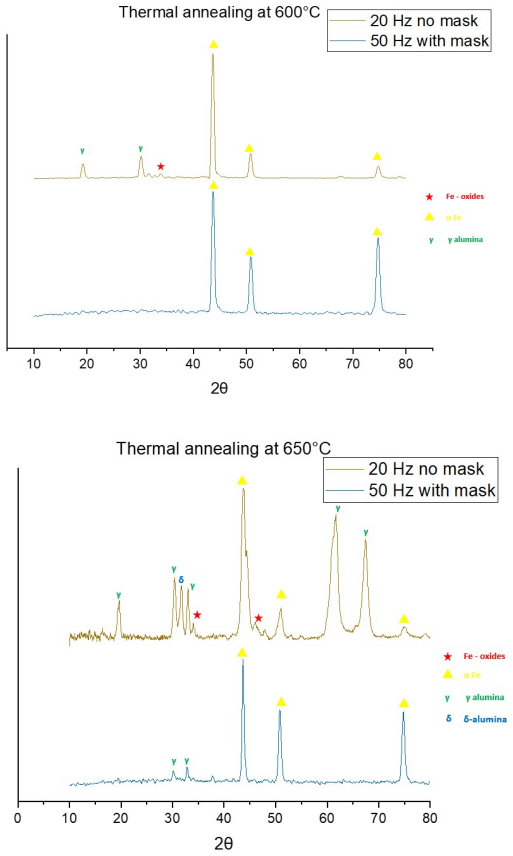

Figure 1: XRD pattern of 600°C and 650°C annealed samples.

that the Al50 exhibits a greater thermal stability. At 600°C it doesn't show any alumina peaks, which weakly arise at 650°C. On the contrary the Al20 even after the first annealing shows an ongoing crystalline phase formation. The trend is confirmed in the 650°C case with stronger peaks and a new arising phase (δ). Furthermore, some weak peaks relative to iron oxides are observable meaning that the integrity of coating is compromised. The SEM images confirm the advanced degree of crystallization, showing numerous fractures induced by the change of phase. After this primary evaluation of the evolution of the crystallization process, the density of the films is obtained through XRR and Spectroscopic Ellipsometry techniques.

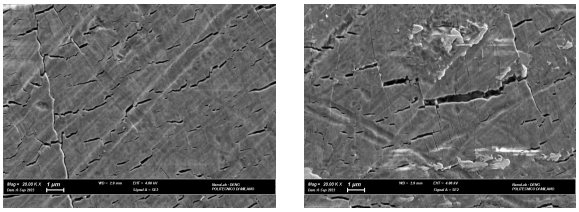

Figure 2: SEM images of the Al20 surface after the annealing process at 650°C for 12 hours.

2.1.1 Density extrapolation

Firstly, the X-ray reflectivity technique is exploited to retrieve the critical angle relative to each sample. The calculation of the density from the critical angle starts from considering the refractive index relative to X-ray and the Snell–Descartes law:

$$n_0 \cdot cos\theta_i = n_1 \cdot cos\theta_t \tag{1}$$

$$n = 1 - \delta - i\beta \tag{2}$$

In the expression of the refractive index, the dissipative imaginary contribute (β) is neglected, considering only the disperisive real part (δ). Adopting the approximation $\theta_c \approx \sqrt{2\delta}$, since only small angles are involved, the density is calculated retrieving the electron density:

$$\rho_e = \frac{\delta \cdot 2\pi}{\lambda^2 \cdot r_e} \tag{3}$$

$$\rho_m = \frac{\rho_e \cdot A}{N_A \cdot Z} \tag{4}$$

The minima of the first, second and third derivatives of the reflectivity curves are considered as potential critical angle[6].
The first derivative of intensity is deemed unsuitable for determining θ_c because its location falls in the middle of the steep intensity drop. Changes in sample/interface roughness can significantly impact the slope in this region, leading to inaccuracies.
While the second derivative would be appropriate under the assumption of an infinitely large sample, it may be influenced by beam footprint effects for real small samples. Therefore, the third derivative is chosen as it provides a reliable θ_c value that, if it makes physical sense, should be independent of sample size, thickness, or roughness. The density values calculated are reported in the following tables (the order from

top to bottom is 3^{rd}, 2^{nd} and 1^{st} minima critical angle(°)).

Al20					
As Dep		**600°C**		**650°C**	
$2\theta_c$	ρ_m	$2\theta_c$	ρ_m	$2\theta_c$	ρ_m
0.351	1.49	0.316	1.20	0.315	1.20
0.425	2.19	0.364	1.60	0.403	1.97
0.496	2.97	0.467	2.64	0.539	3.51

Table 2: Density values (g/cm^3) extrapolated by XRR measurements for Al20.

Al50					
As Dep		**600°C**		**650°C**	
$2\theta_c$	ρ_m	$2\theta_c$	ρ_m	$2\theta_c$	ρ_m
0.426	2.20	0.331	1.32	0.365	1.61
0.471	2.68	0.396	1.90	0.429	2.22
0.515	3.21	0.511	3.16	0.497	2.99

Table 3: Density values (g/cm^3) extrapolated by XRR measurements for Al50.

It appears evidently a significant deviation from the expected values of alumina density ($\approx 3.6 g/cm^3$). The inconsistency of the data coming from the XRR measurements do not allow any physical consideration, since neither the expected trend from XRD patterns is respected. The problem of this technique arises from the fact that it has its optimal efficiency for thinner film and it strongly dependent on the surface roughness. In this case the roughness of the coatings, coming from the substrate, has the same order of magnitude of the coating thickness itself. Additionally, the formula exploited for the density calculation refers to a charge distribution related to the crystalline cell and, since partially crystallized structures are involved, further uncertainties are introduced. Since the unreliability of the XRR technique, Spectroscopic Ellipsometry is exploited for the density calculation. From this technique, the refractive index of a material can be obtained, then the density is retrieved exploiting the Lorentz-Lorentz equation with reference material the α-alumina:

$$\frac{n^2-1}{n^2+2} = K\rho \tag{5}$$

The peculiarity of the ellipsometry, that can overcome the difficulties encountered in the XRR, is that a fitting procedure is required to retrieve the refractive index. Selecting an appropriate model, the thickness and the roughness of the samples can be well described. The refrac-

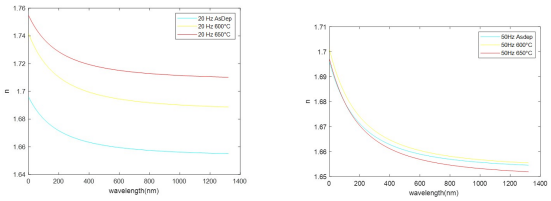

Figure 3: Refractive index of Al20 and Al50 samples in as-deposited conditions and after the thermal annealing at 600°C and 650°C.

tive index relative to the Al20 increases with the temperature. This corresponds to an higher density of the alumina films, meaning a significant extent of crystallization. On the other hand, the Al50 refractive index remains almost constant, suggesting an overall amorphous structure. The values of density, calculated averaging on the wavelength range, are reported in table 4.

	Al20	**Al50**
As Dep	3.591	3.589
600°C	3.742	3.597
650°C	3.825	3.582

Table 4: Density (g/cm^3) extrapolated from ellipsometry measurements for Al20 and Al50 samples.

These two distinct behaviors can be attributed to two deposition parameters: the use of the mask and variations in the deposition rate. The second parameter, the deposition rate, will be investigated after the irradiation experimental part, which involves a set of samples that differ only in terms of this parameter. The mask, located between the target and the substrate, is able to cut off the droplets that have longer pathway in the chamber. During their travelling time, a reorganization of the structure can occur, making the droplets possible nucleation seeds for the crystalline phase.

2.2. Synergic Effect of Irradiation and Temperature

A set of samples, deposited with the characteristics reported in table 5, was sent to IVEM facility to investigate the irradiation effects coupled with thermal process. IVEM facility allows

Al20	Al_2O_3 at 20 Hz with mask
Al50	Al_2O_3 at 50 Hz with mask
AY20	Al_2O_3-Y_2O_3(3%) at 20 Hz with mask

Table 5: Set of IVEM samples.

in-situ experiments involving ion irradiation and ion implantation performed alongside TEM that can simulate the neutron irradiation field inside an LFR. In this context, SRIM software is employed to describe and quantify the irradiation damage in the amorphous structure of the coating. The samples were irradiated with 700 keV Kr^{2+} ions at different temperatures. The TEM images are analyzed to observe the evolution of the alumina structure. In particular, the SAED images are exploited to retrieve the spacing between crystalline planes corresponding to specif phases. From the Dark Field the medium grain size is estimated, while from the bright field the amorphous fraction is obtained. The procedure for each type of images is briefly described.

2.2.1 SAED

Measuring the rings area, the interplanar distances (d-spacing) have been simply calculated and then, comparing with the typical values in literature, each crystalline phase is determined.

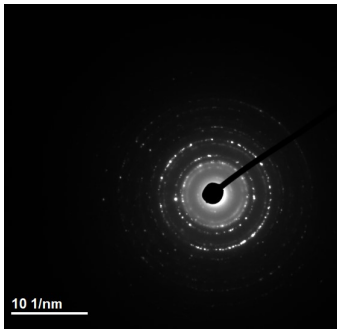

Figure 4: SAED image of Al20 sample at 600°C and 5 dpa.

For a more accurate analysis of the progression, SAED patterns were subjected to a rotational averaging technique, using the DiffTools script within DigitalMicrograph™ software [4]. The patterns obtained for each temperature provide insight into the dpa threshold that initiates the crystallization process.

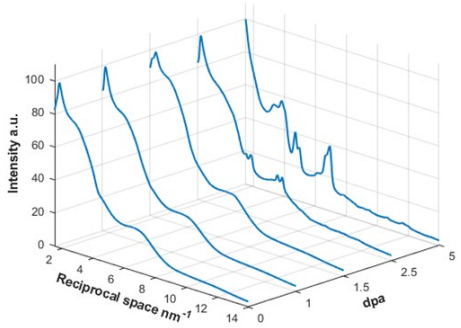

Figure 5: Rotational average pattern of Al20 sample at 600°C and 5 dpa.

2.2.2 Dark Field

Dark field patterns are used to retrieve the trend of the average size of the crystalline grains in the amorphous matrix. The analysis is performed using ImageJ to measure the grain area [5].Once the grain individuated, the area is measured, then approximating it to a sphere shape, the grain size is simply calculated.

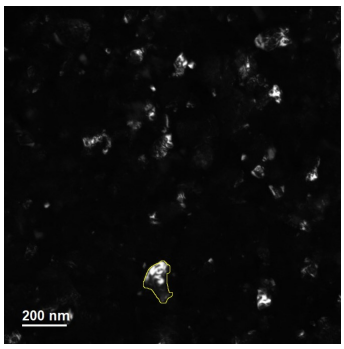

Figure 6: Grain identification procedure through ImageJ in a DF image.

Furthermore, an insight on the crystallization kinetics is given, adopting the Burke and Turnbull model [1]:

$$D_g^n - D_0^n = K(dpa) \tag{6}$$

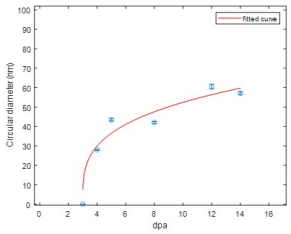

Figure 7: Fitting function of Al50 at 600°C.

2.2.3 Bright Field

The BF analysis is performed using a Matlab able to identify the grains as darker pixels, scanning a range of grays. Then, a value of amorphous fraction is obtained by the ration dark over all pixels.This procedure aims to give a qualitative information about the amorphous fraction, since the significant uncertainty.

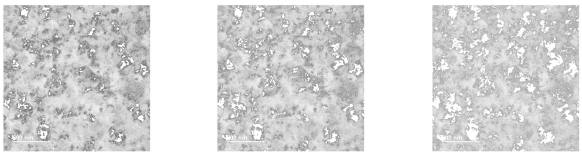

Table 6: This is the procedure followed to retrieve the AF. The uncertainties of this approach arise from the possibility of identification of random darker details in the image as crystalline phases.

2.2.4 Results of IVEM

The Al20 samples are firstly subjected at relatively low temperature to increasing irradiation field, to assess the good radiation endurance of alumina. Indeed, despite of the wide range of dpa values, no evidence of crystalline grains is observable before the temperature of 500°C. This behavior suggest that the crystallization mechanism has to be triggered by thermal effect and the irradiation field constitutes an enhancement factor . The cases with no phase change observable are discarded and the ones analyzed are Al20 at 500°C, 550°C and 600°C, Al50 at 600°C and AY20 at 600°C. Exploiting the SAED patterns, the phase identification procedure is performed and the results are reported in table 7.
The main role of the temperature can be observed from the amorphous fraction progression

	Al20	Al50	AY20
500°C	×	×	×
550°C	γ	×	×
600°C	γ, δ	γ	γ

Table 7: Alumina phases identified for each temperature

at different temperature for the Al20 case. comparing the cases at 550°C and 600°C, a similar amorphous fraction value ($\approx$ 80%) is achieved for the 550°C sample despite experiencing over double the intensity of the irradiation field.

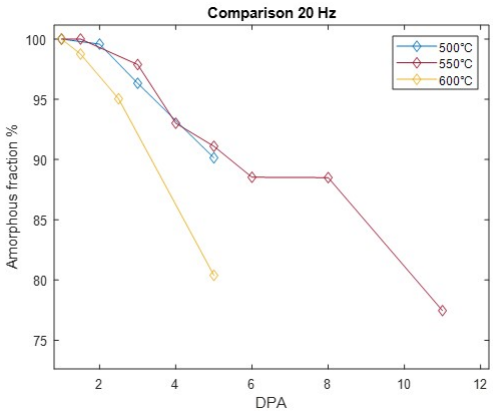

Figure 8: Amorphous fraction comparison of Al20 at different temperatures.

From the Dark field analysis the mean grain size evolution is retrieved for all cases analyzed, allowing a comparison at the temperature of 600°C between the different types of samples as shown in figure 9.
As expected, since the composition of the coatings is identical, the Al20 and Al50 samples show a similar progression in grain size as the dpa values increase. However, a notable difference is observed in the dpa threshold required to initiate the crystallization process, which is higher in the Al50 coating. This phenomenon can potentially be explained by considering the impact of increased pulse repetition rates. In this context, clusters of alumina particles projected onto the substrate have less time to attain an organized crystalline structure due to the higher deposition frequency. According to Li Guan et al. [3], higher deposition frequencies correspond to a greater density of smaller-sized growth islands.

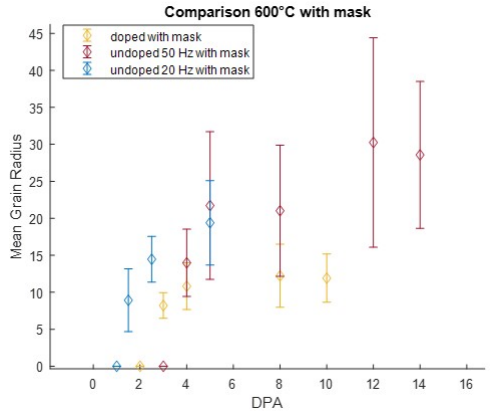

Figure 9: Grain size comparison between all types of samples (Al20, Al50 and AY20) at 600°C.

In the context of an amorphous material, this could result in a lower density of large islands where the reorganization in ordered structure is more likely.
In the AY20 samples, the doping effect results in a significantly smaller mean grain size at all dpa values. This behavior is attributed to the different steric hindrance caused by the presence of yttrium oxide, which impedes the reorganization into a more ordered structure. Although the Bright Field image at 3 dpa indicates an almost complete amorphous structure ($\approx$ 100%), the Dark field image reveals the presence of small grains, indicating that the crystallization process is triggered. This observed evolution aligns with the previous considerations regarding the impact of frequency on the phase change. The same trend observed in the grain size analysis is also evident in the amorphous fraction comparison, as depicted in figure 10.

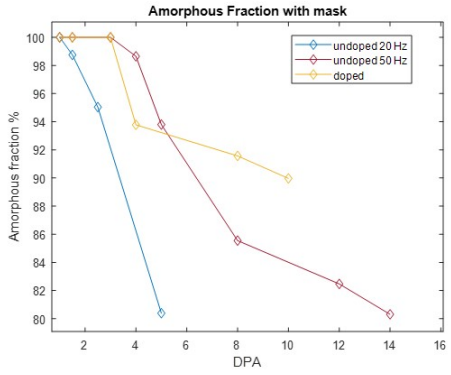

Figure 10: Amorphous fraction comparison of Al20, Al50 and AY20 at 600°C.

3. Conclusions

Since the primary objective was to characterize the materials, spectroscopic ellipsometry has proven to be the most effective technique for investigating this type of films. Its results are physically meaningful and consistent with findings from other performed techniques. The thermal analysis underscores the significance of employing a mask, especially when elevating the deposition rate, to inhibit the initiation of nucleation by long-pathway droplets and the promotion of crystalline phases.
The noted impact of deposition rate implies that higher frequencies contribute to a higher level of disorder within the coating. Nevertheless, it is essential to acknowledge that this effect cannot be disentangled from the influence of the mask, rendering it difficult to distinctly identify the distinct advantages of employing higher deposition frequencies.
The irradiation campaign conducted at the IVEM facility provided valuable insights into the possible extent of radiation damage in the three kind of samples. The expected excellent radiation endurance properties result confirmed, as no evidence of radiation damage was observed before reaching 500°C, temperature close to the operational range of a LFR. The influence of pulse frequency emerged as a significant factor since a higher pulse frequency corresponds to a higher degree of disorder inside the alumina coating. This means that the coating is able to absolve its protection function maintaining its integrity in harder conditions.Additionally, the benefits relatively the Yttria doping are observed suggesting an improved radiation endurance adopting alumina-yttria compounds as coating material.
In conclusion, alumina-based coatings stand out as a strong candidate in the context of Lead-cooled Fast Reactors due to their promising thermal and under-irradiation behavior. However, before their practical application, a more comprehensive characterization is required. Specifically, there is a need for a complete understanding of their mechanical properties and how they perform under prolonged exposure to liquid lead.

References

[1] JE Burke and David Turnbull. Recrystallization and grain growth. *Progress in metal physics*, 3:220–292, 1952.

[2] F García Ferré, A Mairov, Daniele Iadicicco, Matteo Vanazzi, S Bassini, M Utili, M Tarantino, M Bragaglia, FR Lamastra, F Nanni, et al. Corrosion and radiation resistant nanoceramic coatings for lead fast reactors. *Corrosion Science*, 124:80–92, 2017.

[3] Li Guan, DuanMing Zhang, Xu Li, and Zhi-Hua Li. Role of pulse repetition rate in film growth of pulsed laser deposition. *Nuclear Instruments and Methods in Physics Research Section B: Beam Interactions with Materials and Atoms*, 266(1):57–62, 2008.

[4] David RG Mitchell. Difftools: Electron diffraction software tools for digitalmicrograph™. *Microscopy research and technique*, 71(8):588–593, 2008.

[5] Caroline A Schneider, Wayne S Rasband, and Kevin W Eliceiri. Nih image to imagej: 25 years of image analysis. *Nature methods*, 9(7):671–675, 2012.

[6] Sjoerd A Veldhuis, Peter Brinks, Tomasz M Stawski, Ole F Göbel, and Johan E ten Elshof. A facile method for the density determination of ceramic thin films using x-ray reflectivity. *Journal of sol-gel science and technology*, 71:118–128, 2014.